Renewable and Sustainable Energy Reviews 150 (2021) 111497

Contents lists available at ScienceDirect

Renewable and Sustainable Energy Reviews

journal homepage: www.elsevier.com/locate/rser

Experimental investigation on performance improvement by mid-plane guide-vanes in a biplane-rotor Wells turbine for wave energy conversion

João S. Alves [a], Luís M.C. Gato [b,*], António F.O. Falcão [b], João C.C. Henriques [b]

[a] Royal Institute of Technology, SE-100 44, Stockholm, Sweden
[b] IDMEC, Instituto Superior Técnico, Universidade de Lisboa, Av. Rovisco Pais 1, 1049-001 Lisbon, Portugal

ARTICLE INFO

Keywords:
Wells turbine
Air turbine
Biplane
Guide vanes
Wave energy
Oscillating water column

ABSTRACT

The Wells turbine is the most frequently used or proposed self-rectifying air turbine for oscillating-water-column wave-energy converter application, largely because of its conceptual and mechanical simplicity. Biplane Wells turbines allow a higher total blade solidity to be attained than monoplane turbines do, but this results in larger aerodynamic losses associated with the swirl kinetic energy loss at turbine exit. This may be overcome by the presence of a row of guide vanes between the two rotor planes, a solution that had been proposed and investigated theoretically or by numerical modelling. Results of turbine overall performance and flow details are reported from laboratory tests of a biplane Wells turbine without guide vanes and with specially designed guide vanes. The presence of the guide vanes was found to increase the peak efficiency by seven percentual points, while reducing (for fixed rotational speed) the damping provided by the turbine. Measured losses in the guide vane row were much smaller than in the rotors. Experimental results are compared with previously published numerical results. A stochastic theoretical transform was applied to obtain averaged results for the turbine performance subject to the irregular bidirectional air flow induced by real sea waves.

1. Introduction

The conversion of sea wave energy into useable, mostly electrical, energy has been object of extensive research and development activity in many countries, especially since the 1970s [1]. Among the wide variety of wave energy conversion concepts, the oscillating water column (OWC) has been regarded by many developers as the simplest and most reliable technology. It is the one with the largest number of prototypes deployed into the sea [1–4]. It consists of a fixed or floating hollow structure open to the sea at its submerged part, inside which the air trapped in an air chamber above the inner free-surface is alternately compressed and decompressed by wave action. In most cases, the air chamber is directly connected to the atmosphere through an air turbine whose rotational direction remains unchanged regardless of the direction of the air flow. Two basic types of such self-rectifying air turbines were invented and patented in the mid-1970s: the Wells turbine [5] and the axial-flow impulse turbine [6]. Reviews of these two types of air turbines and other types may be found in Refs. [3,7–13].

The Wells turbine is an axial-flow turbine that is particularly attractive for its conceptual and mechanical simplicity. In its simplest version, the turbine has no guide vanes and the rotor blades are shaped as symmetrical aerofoils whose chordal plane is perpendicular to the rotational axis (Fig. 1). In the absence of guide vanes, the flow velocity at rotor exit has a non-zero swirling component, whose kinetic energy is not recovered. Such a loss penalizes the turbine efficiency. This can be overcome by equipping the turbine with appropriately designed guide vanes. Since the flow is bidirectional and the turbine should be insensitive to the flow direction, there must be two rows of guide vanes, one on each side of the rotor, that are the mirror image of each other with respect to a plane perpendicular to the rotational axis (Fig. 1).

For fixed inner and outer radii, and given flow rate and rotational speed, it is known that the flow deflection produced by the rotor blades and hence also the torque and the power of the turbine increase with the total bladed area [13]. This may be important in applications where the pressure head available to the turbine is relatively large, as occurs in the more energetic sea states or in special OWCs like the spar-buoy OWC [14]. Obviously, in a rotor with a single row of blades, the solidity (total bladed area divided by the annular area) must be smaller than, and not too close to, unity. The setting of the rotor blades onto two planes – the biplane Wells turbine – was proposed in Ref. [15], where results from testing of a small biplane Wells turbine model without guide vanes are reported. This type of turbine equipped the shoreline OWC prototype on the island of Islay (Scotland, UK), completed in

* Corresponding author.
E-mail addresses: joaosa@kth.se (J.S. Alves), luis.gato@tecnico.ulisboa.pt (L.M.C. Gato), antonio.falcao@tecnico.ulisboa.pt (A.F.O. Falcão), joaochenriques@tecnico.ulisboa.pt (J.C.C. Henriques).

https://doi.org/10.1016/j.rser.2021.111497
Received 16 October 2020; Received in revised form 7 July 2021; Accepted 8 July 2021
Available online 27 July 2021

Nomenclature

Romans

A	Duct cross-sectional area [m^2]
c	Blade chord [m]
c_D	Drag coefficient [–]
c_L	Lift coefficient in cascade [–]
c_{L_0}	Lift coefficient for an isolated airfoil [–]
D	Rotor diameter [m]
E	Work per unit mass of fluid [m^2/s^2]
$\dot{E}$	Energy per unit time [W]
G	Gap between rotor planes [m]
k_f	Cascade influence factor [–]
K	Ψ/Φ [–]
L	Duct length [m]
p	Pressure [Pa]
p_0	Total pressure [Pa]
P_{avail}	Available power [W]
P_{loss}	Power loss [W]
Q	Volume flow rate [m^3/s]
r	Radial coordinate [m]
R	Rotor radius [m]
Re	Reynolds number [–]
t	Cascade pitch (Section 2) [m]
t	Time [s]
T	Torque [Nm]
u	Uncertainty [–]
$\mathbf{U}$	Blade velocity [m/s]
$\mathbf{V}$	Absolute flow velocity [m/s]
$\mathbf{W}$	Relative flow velocity [m/s]
Z	Number of rotor blades [–]
z^*	Dimensionless spanwise coordinate [–]

Greek symbols

α	Angle of the absolute velocity vector [–]
α'	Guide-vanes metal angle [–]
β	Angle of the relative velocity vector [–]
γ	Angle defining the camber, Fig. 6 [–]
Δp	Pressure head [Pa]
η	Total-to-static efficiency [–]
η^*	Eq. (32) [–]
λ	Loss coefficient, Eq. (33) [–]
Λ	Loss coefficient, Eq. (31) [–]
μ	Dynamic viscosity [Pa s]
Π	Torque coefficient, Eq. (19) [–]
ρ	Density [kg/m^3]
σ	Standard deviation of Δp [Pa]
σ_Ψ	Standard deviation of Ψ [–]
τ	Time interval [s]
ϕ	Flow coefficient, Eq. (4) [–]
Φ	Flow coefficient, Eq. (17) [–]
ψ	Pressure head coefficient, Eq. (4) [–]
Ψ	Pressure head coefficient, Eq. (19) [–]
ω	Wave angular frequency [rad/s]
Ω	Rotational speed [rad/s]

Subscripts

at	Atmospheric value
GV	Guide vanes, turbine with guide vanes
hub	Value at the hub
noGV	Turbine without guide vanes
pl	Plenum chamber value
R1	Rotor 1
R2	Rotor 2
x	Axial component
θ	Circumferential component

1990 [16], and also the 16 OWCs of the breakwater at Mutriku harbour (Basque Country, Spain) [17]. A turbine similar to those of Mutriku was installed in 2016 at the OWC-breakwater of Civitavecchia (Italy) [18].

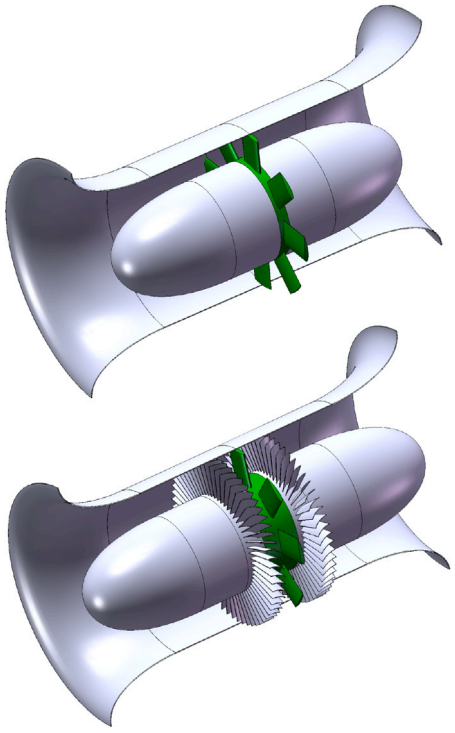

Fig. 1. Monoplane Wells turbine without guide vanes (above) and with guide vanes (below).
Source: Courtesy of R.P.F. Gomes.

The reduction in Wells turbine efficiency due to swirl exit velocity should be expected to be more significant for higher rotor blade solidities (and larger work per unit mass of fluid), since (in the absence of guide vanes), from Euler turbine equation, the work per unit mass of fluid is proportional to the circumferential component of the exit velocity, whereas the swirl kinetic energy is proportional to the square of that velocity. For this reason, the improvement in turbine efficiency provided by guide vanes should be especially relevant in the case of the biplane Wells turbine, at least as far as the total blade solidity allowed by the biplane exceeds what would be possible to accommodate in a monoplane rotor. Curiously, none of the biplane Wells turbines at the Islay, Mutriku and Civitavecchia OWCs (see above) is or was equipped with guide vanes. This may be explained by the option of avoiding the additional mechanical complexity and cost of the guide vanes.

Alan Arthur Wells (1924–2005) was a distinguished academic and professor at Queen's University of Belfast. The development of his turbine was done at Queen's essentially by his colleague S. Raghunathan and co-workers who carried out, since about 1980, extensive research and development work on the Wells turbine, including detailed experimental work. This, together with work by other groups, is reported in

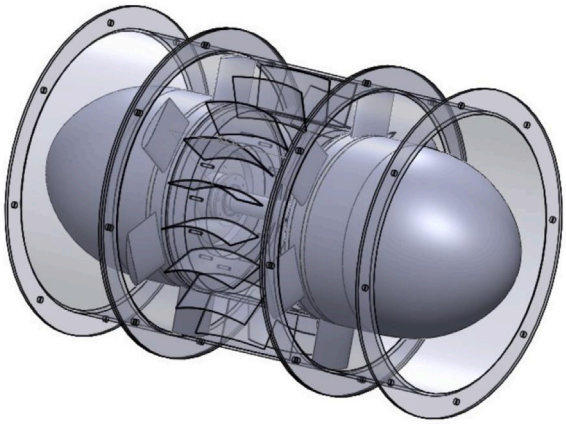

Fig. 2. Biplane Wells turbine with symmetric guide-vane row between rotor planes.

Raghunathan's long and detailed review paper [7] published in 1995. A substantial part of that paper is devoted to the biplane Wells turbine, including the effect of a pair of guide-vane rows, one on each side of the biplane rotor.

The effect of solidity upon the efficiency of Wells turbines without guide vanes was investigated experimentally in Ref. [19] (see also Ref. [13]), with different settings (mono- and biplane) and number of identical blades (8 or 16, solidities 0.64 and 1.28). The peak efficiencies were found to be 0.59 for the 8-bladed monoplane, 0.62 for the biplane with 4+4=8 blades and only 0.52 for the biplane with 8+8=16 blades. This should be compared with 0.71 for the peak efficiency of the 8-bladed monoplane with guide vanes. (No tests were performed for the biplane turbines with guide-vanes.) These values show that the peak-efficiency of turbines without guide-vanes is severely affected by increasing solidity and that the presence of guide-vanes should be expected to allow a significant increase in efficiency, especially in the case of high-solidity biplanes. This confirms the earlier findings of Raghunathan [7].

Published information on measured performance of a biplane Wells turbine with two rows of guide vanes, one of each side of the biplane rotor, can be found in Ref. [7].

An alternative configuration consists in setting the guide vanes in a single row located between the two planes of the rotor. In this case, the guide vanes should be symmetrical with respect to a plane perpendicular to the rotational axis (Fig. 2), and should be cambered.

Experimental results comparing the performances of biplane Wells turbines (i) without guide vanes, (ii) with a pair of guide-vane rows, and (iii) with a single guide-vane row between rotor planes can be found in Ref. [20], published in 1990. Unfortunately, in (iii), the intermediate guide vanes were shaped as flat plates rather than suitably cambered plates to match the swirling flow from the upstream rotor and the angle of the flow that should be admitted to the downstream rotor. This negatively affected the performance of the turbine (iii) in comparison with the twin-guide-vane-row biplane turbine (ii) with cambered inlet and outlet guide vanes.

The concept of a single guide-vane row between rotor planes later appeared in patent Ref. [21], and was subsequently analysed theoretically in Ref. [11] and numerically with a Computational Fluid Dynamics (CFD) code in Ref. [22]. It is the main subject of the present paper.

A two-dimensional analysis, based on irrotational incompressible flow, is presented in Section 2 for single-plane and biplane Wells turbines with and without guide vanes. The aerodynamic design of the guide vanes is described in Section 3. This is followed, in Sections 4 and 5, by the description of the turbine construction and of the experimental setup, respectively. Experimental results and their comparison with published numerical results are given in Section 6. Unidirectional versus bidirectional flow testing is discussed in Section 7, followed by time-averaged turbine-performance evaluation in irregular-wave-induced air flow. Conclusions appear in Section 8.

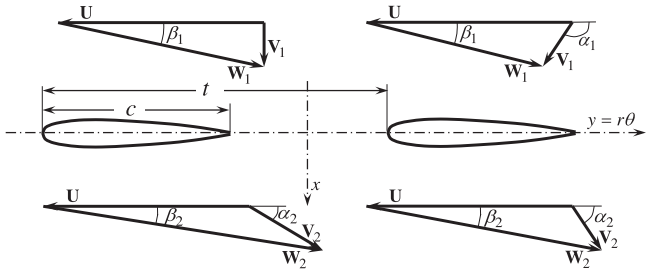

Fig. 3. Two-dimensional flow about a Wells turbine rotor. On the left: velocity diagrams with no swirl upstream of the rotor; on the right: velocity diagrams with swirl upstream of the rotor.

2. Two-dimensional flow analysis

The flow through a turbomachine is very complex, especially if fixed vanes and moving blades are present, as in the present case. A simplified two-dimensional approach to the Wells turbine, based on incompressible irrotational flow, is adopted here. This may provide, in a relatively simple way, insights into the dynamics of the turbine, its flow and the design of blades and vanes. The method is based on conformal transformation, and has been applied to model the flow through monoplane Wells turbines without guide vanes [23] and with guide vanes [24]. It was later generalized to biplane Wells turbines [11].

In the simplified two-dimensional model adopted here, it is assumed that: (i) the real three-dimensional flow may be represented by a set of two-dimensional plane cascade flow patterns, each resulting from the development onto a plane of the corresponding streamsurface assumed circular cylindrical of radius r; (ii) in the two-dimensional cascade flow, the flow velocity is assumed to be approximately uniform upstream (vector $\mathbf{V}_1$) and downstream (vector $\mathbf{V}_2$) of the blades that move with velocity $\mathbf{U}$ ($U = \Omega r$ where Ω is rotational speed in radians per unit time). The relative flow velocity vector is $\mathbf{W} = \mathbf{V} - \mathbf{U}$. Fig. 3 shows a plane cascade of Wells turbine rotor blades, with the velocity vectors and their angles α and β. In the figure, c is the blade chord and $t = 2\pi r/Z$ (Z = number of rotor blades) is the cascade pitch.

In order to use conformal transformation techniques, the cascade flow is assumed incompressible and irrotational. If the blades are uncambered and their thickness is neglected, an exact analytical solution is available for the flow about a plane cascade of flat blades [25–28]. In the present case, in which the angle of stagger is 90°, it can be found (see Ref. [11,24]) that

$$\cot \alpha_2 = \cot \alpha_1 + 2 \tan \frac{\pi c}{2t}. \tag{1}$$

This equation shows that the angle α_2 of the absolute velocity vector $\mathbf{V}_2$ at rotor exit depends only on inlet angle α_1 and on chord-to-pitch ratio (cascade solidity) c/t, not on flow rate or on blade velocity.

The work done by the moving blades per unit mass of fluid can easily be obtained and is

$$E = 2\Omega r V_x \tan \frac{\pi c}{2t}, \tag{2}$$

where $V_x = V_1 \sin \alpha_1 = V_2 \sin \alpha_2$ is the axial component of the flow velocity (upstream or downstream of the cascade). This shows that, for given V_x and blade velocity Ωr, the work E per unit mass of fluid is independent of the angle α_1 of the inlet flow velocity. Assuming perfect fluid, the pressure drop across the cascade is

$$\Delta p_{12} = p_1 - p_2 = \frac{\rho}{2}(W_2^2 - W_1^2). \tag{3}$$

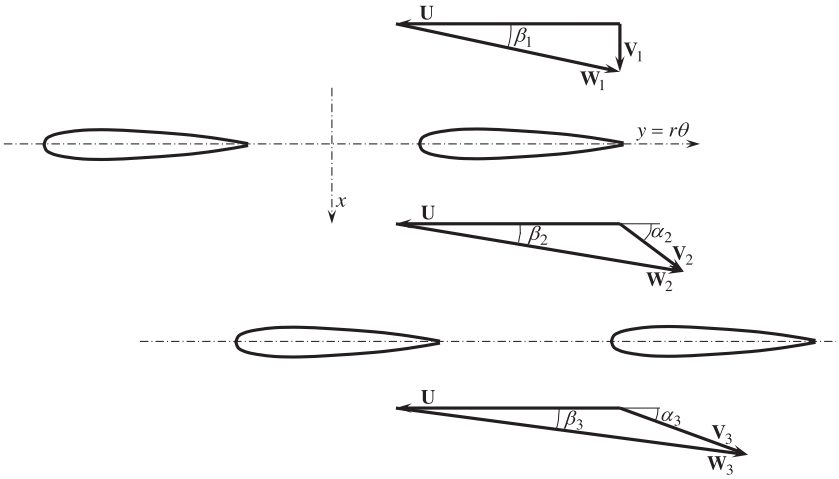

Fig. 4. Two-dimensional flow about a biplane rotor Wells turbine without guide vanes.

We introduce the variables

$$\phi = \frac{V_x}{\Omega r}, \quad \psi = \frac{\Delta p}{\rho \Omega^2 r^2}, \tag{4}$$

that may be regarded as dimensionless coefficients of flow rate and pressure head, respectively.

2.1. Biplane without guide vanes

We consider now the biplane Wells turbine without guide vanes, the spacing between planes being assumed large enough for the flow upstream of the second plane to be approximately uniform. The blades and the number of blades are equal on both planes. The two-dimensional cascade is represented in Fig. 4. In this case, it is $\alpha_1 = \pi/2$ at the entrance to the first row of rotor blades. It may be found that the work per unit mass done by the twin rows of rotor blades is

$$E = E_{12} + E_{23} = 4\Omega r V_x \tan\frac{\pi c}{2t}, \tag{5}$$

since $E_{12} = E_{23}$, see Eq. (2). The dimensionless pressure drop is

$$\psi_{12} = 2\phi\left(1 + \phi\tan\frac{\pi c}{2t}\right)\tan\frac{\pi c}{2t} \tag{6}$$

across the first row of rotor blades, and

$$\psi_{23} = 2\phi\left(1 + 3\phi\tan\frac{\pi c}{2t}\right)\tan\frac{\pi c}{2t} \tag{7}$$

across the second row, with

$$\psi = \psi_{12} + \psi_{23} = 4\phi\left(1 + 2\phi\tan\frac{\pi c}{2t}\right)\tan\frac{\pi c}{2t} \tag{8}$$

for the biplane turbine. Eqs. (6) and (7) show that the second row of rotor blades requires a larger pressure drop than the first row to perform the same work.

The (total-to-static) efficiency is

$$\eta = \frac{E}{\dfrac{p_1 - p_3}{\rho} + \dfrac{V_x^2}{2}} \tag{9}$$

or

$$\eta = \frac{1}{1 + 2\phi\tan\dfrac{\pi c}{2t} + \dfrac{\phi}{8}\cot\dfrac{\pi c}{2t}}\,. \tag{10}$$

2.2. Biplane with intermediate guide vanes

The kinetic energy per unit mass of fluid at the exit of the last row of blades or of guide vanes is assumed lost. This is aggravated if swirl is present, as is the case of the biplane rotor without guide vanes shown in Fig. 4. The exit swirl can be reduced by the appropriate use of guide vanes. Account has to be taken that the turbine should be insensitive to flow direction, and so the whole set of rotor blades and guide vanes has to be symmetrical with respect to a plane perpendicular to the rotational axis. In the case of a biplane rotor, two guide vane topologies may be considered [7,11,20]: (i) two rows of guide vanes, one on each side of the biplane rotor, and (ii) a row of guide vanes between the two rotor planes. The latter topology is considered here. The corresponding plane cascade is shown in Fig. 5. It is assumed that the axial distance between the three cascades is large enough for the flow upstream of the guide vanes and upstream of the second rotor to be approximately uniform. Since $\alpha_1 = \pi/2$, Eq. (1) determines that

$$\cot\alpha_2 = 2\tan\frac{\pi c}{2t}. \tag{11}$$

If the flow at turbine exit is to be swirl-free, it must be $\alpha_4 = \pi/2$. From Eq. (1), it follows that

$$\alpha_3 = \pi - \alpha_2. \tag{12}$$

The dimensionless pressure head ψ is proportional to the dimensionless flow rate ϕ

$$\psi = \psi_1 + \psi_2 = 4\phi\tan\frac{\pi c}{2t}. \tag{13}$$

By comparing Eqs. (8) and (13), it may be concluded that the presence of the guide vanes decreases the derivative $\mathrm{d}\psi/\mathrm{d}\phi$.

The efficiency is given by

$$\eta = \frac{1}{1 + \dfrac{\phi}{8}\cot\dfrac{\pi c}{2t}}\,. \tag{14}$$

Comparison with Eq. (10) shows the increase in efficiency due to the presence of the guide vanes.

The guide vanes are to be designed to match conditions (11) and (12). Note that α_2 and α_3 depend only on the chord-to-pitch ratio c/t and not on flow rate or on rotational speed. In bidirectional flow, both edges of the guide vanes act alternately as leading edge and trailing edge, and so they should be sharp. A way of reducing the costs is to use curved metal plate to fabricate the guide vanes. This option is adopted here, with circular-arc guide vanes.

The design method is based on the conformal mapping of the potential incompressible flow about a circle onto the flow about a rectilinear cascade of circular-arc aerofoils (see Ref. [27]). The Kutta condition applies at the trailing edge, and the direction of the incoming flow is assumed such that the velocity at the leading edge is finite (this is known as shock-free conditions, see Ref. [27]). In the case under consideration here (Fig. 5), the stagger angle of the guide-vane cascade is zero. If condition (12) is to be met, then the cascade geometry must

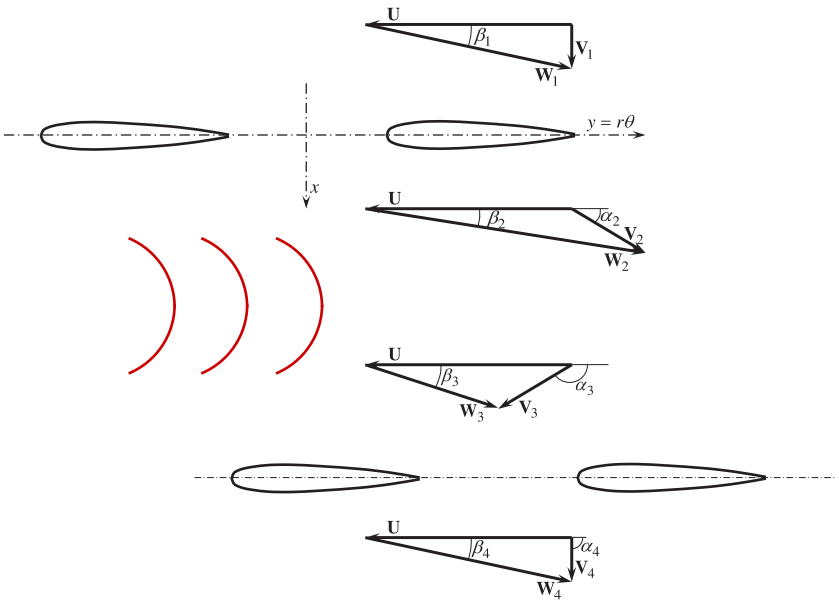

Fig. 5. Two-dimensional flow about a biplane rotor Wells turbine with intermediate guide vanes.

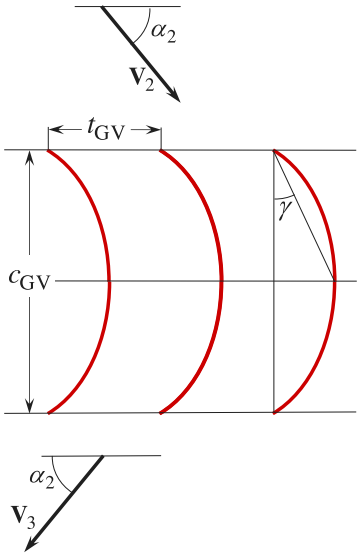

Fig. 6. Cascade of circular-arc aerofoils under shock-free conditions.

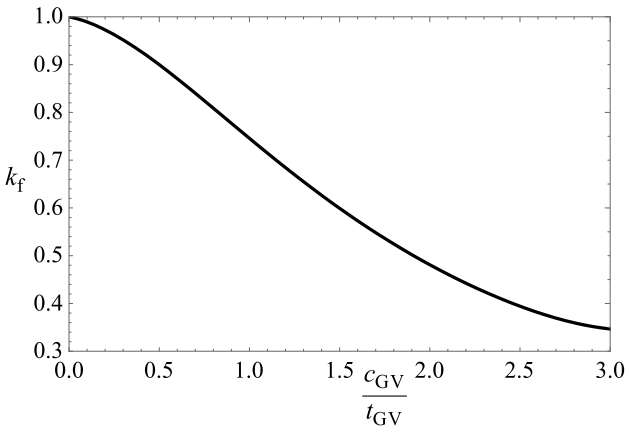

Fig. 7. Influence factor for unstaggered cascade of circular-arc aerofoils and shock-free flow.
Source: Adapted from [27].

be such that both edges of the guide vanes are points of finite velocity. In order to find such geometry, an influence factor is defined as

$$k_f = \frac{c_L}{c_{L_0}}, \tag{15}$$

where c_L is the lift coefficient of the circular-arc aerofoil in cascade and c_{L_0} is the lift coefficient of an identical isolated aerofoil, in both cases under shock-free conditions. It is well known (see e.g. Ref. [25]) that, for the isolated circular-arc aerofoil under shock-free conditions (i.e. for zero angle of attack with respect to the chord direction), it is $c_{L_0} = 2\pi \tan\gamma$, where γ is the angle defining the camber (see Fig. 6) (it is $\gamma = \theta/4$ where θ is the curvature of the circular-arc aerofoil). The lift coefficient for the aerofoils in the cascade configuration and shock-free flow, as shown in Fig. 6, is (see e.g. Ref. [29])

$$c_L = 4\frac{t_{GV}}{c_{GV}} \cot\alpha_2, \tag{16}$$

where the subscript GV stands for guide vanes. The influence factor k_f for the unstaggered cascade of circular-arc aerofoils and shock-free flow is plotted in Fig. 7 versus c_{GV}/t_{GV}.

3. Aerodynamic design of the guide vanes

The turbine whose tests are reported here was a biplane Wells turbine with intermediate guide-vanes. Each rotor had four blades of NACA 0015 profile, of constant chord along the blade span (see Table 1). The two rotors had been used in previous experimental investigations of biplane Wells turbines without guide vanes [19,30]. In Ref. [30], it was found that the circumferential position of one rotor with respect to the other one may considerably affect the turbine performance curve if the gap G between rotor planes was small, $G = 0.5c = 62.5$ mm, but not for $G = 1.4c = 175$ mm. In the present case, the two rotors were mounted so that each one was the image of the other one with respect to a plane perpendicular to the rotational axis. Since the axial distance between rotor planes was $G = 350$ mm, it was reasonable to assume that the circumferential position of one rotor with respect to the other one did not significantly affect the turbine performance.

Table 1
Rotor specification.

Outer casing diameter [m]	0.590
Hub diameter [m]	0.400
Inner-to-outer diameter ratio	0.678
Blade profile	NACA 0015
Blade chord [m]	0.125
Number blades in each rotor	4
Rotor solidity at hub	0.395

Table 2
Flow angles and geometric data for the intermediate guide vanes.

r/R	0.678	0.742	0.807	0.871	0.936	1
α_2 [°]	44.5	48.8	52.1	54.9	57.2	59.1
α_3 [°]	135.5	131.2	127.9	125.1	122.8	120.9
α'_2 [°]	36.6	40.5	43.6	46.1	48.3	50.2
α'_3 [°]	143.4	139.5	136.4	133.9	131.7	129.8
c_{GV}/t_{GV}	2.66	2.31	2.02	1.79	1.60	1.44
c_{GV} [m]	0.176	0.167	0.159	0.152	0.146	0.141

A quasi-three-dimensional-flow turbine design code was used to determine the required radial distribution of the absolute flow angles at the inlet to, and exit from, the intermediate guide-vanes for the given geometry of the rotors. The design method combined an axisymmetric throughflow numerical calculation based on the streamline curvature method [31] and two-dimensional cascade data [32]. This method is widely used in turbomachinery preliminary design before starting a more detailed CFD analysis [31]. The streamline curvature method gives the solution of the Euler equations assuming axisymmetric flow through turbomachinery stages. Because the solution of inviscid-flow Euler equations is incapable of predicting entropy rises in subsonic flow, the method was combined with cascade flow prediction methods [32] to estimate losses and flow angles at the blading exit. In design conditions, the flow should be swirl-free downstream of the second rotor. The numerical scheme considered a simple structured mesh defined by 11 quasi-streamlines assumed closely aligned with the flow direction and 13 quasi-normals. The two rotor-blade rows and the guide-vane row were represented by actuator-discs at three quasi-normals representing the outlet conditions from the rotors and guide-vanes rows. The streamline curvature throughflow calculation gave the flow field velocity and pressure distributions whereas the jumps in pressure and circumferential velocity component at each rotor disc were given, for each radius, from two-dimensional cascade data. Furthermore, symmetry imposed that the flow angles at the inlet to, and exit from, the intermediate stator are given by Eq. (12). Viscous losses were neglected at the guide-vanes. The flow field depends on the radial distribution of the drag-to-lift ratio of the rotor-blade sections, $c_D(r)/c_L(r)$, which is function of the relative flow incidence angle distributions, $\beta_1(r)$ and $\beta_3(r)$ (see Fig. 5). Since the turbine is to be subject to time-varying flow, shock-free inlet flow conditions at the intermediate guide-vanes row will occur only at the design non-dimensional flow coefficient. Weak dependence on the flow coefficient is expected to occur within the rotor high-efficiency stall-free range, which corresponds to small c_D/c_L [24].

We define the dimensionless flow-rate coefficient of the turbine as

$$\Phi = \frac{Q}{\Omega D^3}, \tag{17}$$

where Q is the volume flow rate and $D = 2R$ is the turbine rotor diameter. Table 2 presents the results for the flow angle distributions $\alpha_2(r/R)$ and $\alpha_3(r/R)$ for the flow through the turbine with a row of 19 guide vanes (angles α_2 and α_3 are defined as in Fig. 5). This was computed for $\Omega = 308.9$ rad/s, $Q = 1.8\,m^3/s$ and $\Phi = 0.0284$.

Once the flow angle distributions $\alpha_2(r)$ and $\alpha_3(r)$ were known, the geometry of the circular-arc guide-vanes could be defined by combining the Zweifel criterion [31] with the two-dimensional theory of Section 2.2. The results are given in Table 2, where α'_2 and $\alpha'_3 = 180° - \alpha'_2$ are metal angles at the edges of the guide vanes. From trigonometry, it is

$$\tan\gamma = \frac{1-\cos\alpha'_2}{\sin\alpha'_2}, \tag{18}$$

where γ is the angle represented in Fig. 6 (it is $\gamma = \theta/4$, where θ is the curvature of the circular-arc aerofoil).

The total guide-vane cylindrical surface area (19 vanes) divided by the annular area is 2.17.

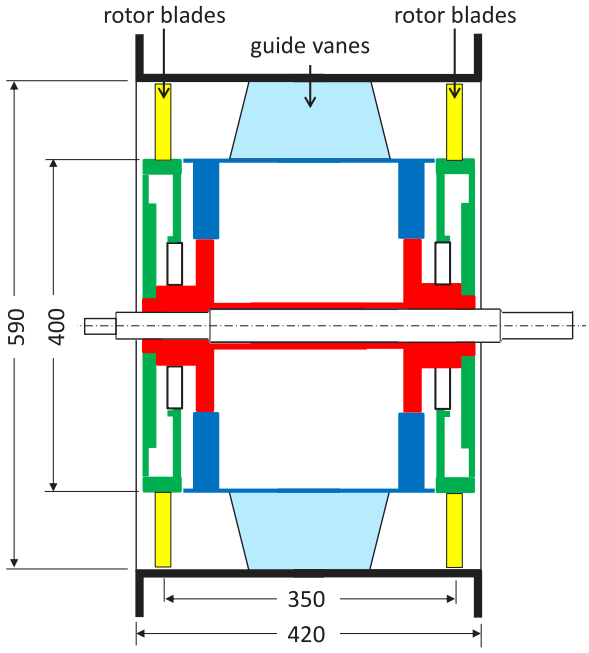

Fig. 8. Turbine longitudinal section (dimensions in mm).

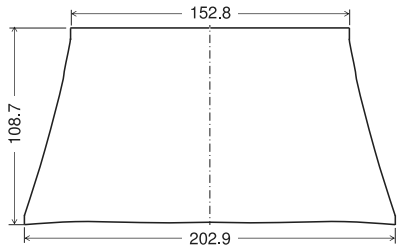

Fig. 9. Two-dimensional guide-vane geometry prior to roll bending (dimensions in mm).

4. Turbine construction

The turbine annular cross-section had inner and outer diameters equal to 0.400 m and 0.590 m, respectively (Fig. 8).

There were four rotor blades on each of the two planes. They were made of aluminium, with NACA0015 symmetric profile and constant chord equal to 0.125 m. Blade tip clearance was less than 1 mm. The axial distance between the planes of symmetry of the two rotor blade rows was 0.350 m.

The 19 guide vanes were made of St37-2 steel plate of 2 mm thickness. As explained in Section 3, they were designed to have single curvature as if cut from a circular cylindrical surface of radius 0.123 m. Fig. 9 shows the two-dimensional guide-vane geometry prior to roll bending.

The hub and the outer casing between rotors were made of 6 mm-thick St37-2 steel plate. Both the hub and the casing were divided into

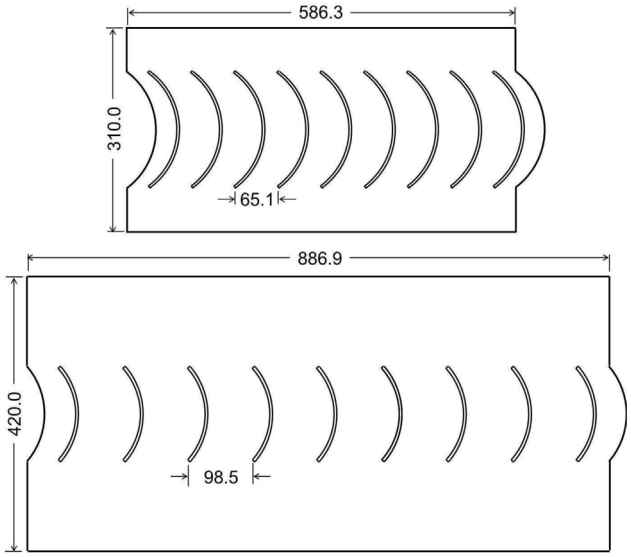

Fig. 10. Two-dimensional geometry of hub and casing parts holding 9 guide vanes (dimensions in mm).

two unequal parts, one holding 9 vanes and the other one holding 10 vanes. So that the guide vanes could be accurately positioned, 3 mm-wide slots of appropriate curvature and length were cut into the hub and casing plates, before roll-bending, by a computer-assisted laser cutting process (see Fig. 10). The hub and casing steel plates were bended in a roll-forming process until they featured the desired radii. The guide vanes were manufactured in a similar way. A two-dimensional drawing of the blade was made, so that it could be laser-cut and roll-bended afterwards. The guide vanes in their final shape were radially inserted into the turbine through the slots in the casing until they reached the hub, after which the vanes, casing and hub could be welded together piece by piece.

Obviously, the configuration without guide vanes was different. In order to link and uphold the casing, eight steel rods of 10 mm diameter were placed onto two cross-planes at 90° degree spacing on each plane.

5. Experimental setup

5.1. Test rig

The turbine was tested in unidirectional flow at the blow-down test rig of the Turbomachinery Laboratory of Instituto Superior Técnico, in Lisbon (Fig. 11). The air was flowing from the atmosphere into the turbine through an annular cylindrical inlet duct, Fig. 12. The turbine rotor was coupled, inside its extended hub, to a Siemens electrical motor/generator through a torque transducer. The turbine was connected by a diffuser to a plenum chamber made of wood, 2.0 m long, 1.7 m high and 1.8 m wide. Inside the chamber there was a flow-straightening honeycomb made of 30 mm diameter pipes separating the two sides of

Fig. 12. Turbine model.

Fig. 13. Traverse probe mechanism.

the chamber. The downstream part of the chamber was connected to a fibreglass calibrated convergent nozzle of inlet diameter 0.800 m that gradually decreased to 0.400 m over a length of 0.670 m. The nozzle was connected by a conical duct to a centrifugal fan responsible for sucking the air into the turbine. The air flow rate through the turbine was controlled by adjusting the rotational speed of the fan.

Wall pressure taps were located at the upstream (4) and downstream (5) parts of the plenum chamber, and (6) at the smallest section of the convergent nozzle used for flow rate measurements.

To determine the yaw angle of the flow velocity, a traverse moving three-hole probe with two degrees of freedom was used, Figs. 13 and 14. The probe had two degrees of freedom: translational motion along its own axis in the radial direction and rotation around its axis. These motions were controlled by the probe own unit in which both radial position and yaw angle were indicated. The length of the probe was

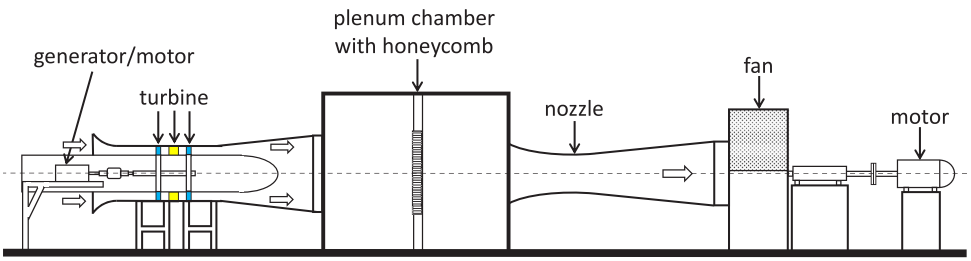

Fig. 11. Blow-down test-rig.

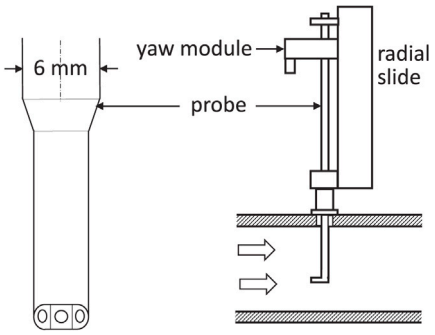

Fig. 14. Schematic representation of the three-hole probe and traverse probe mechanism.

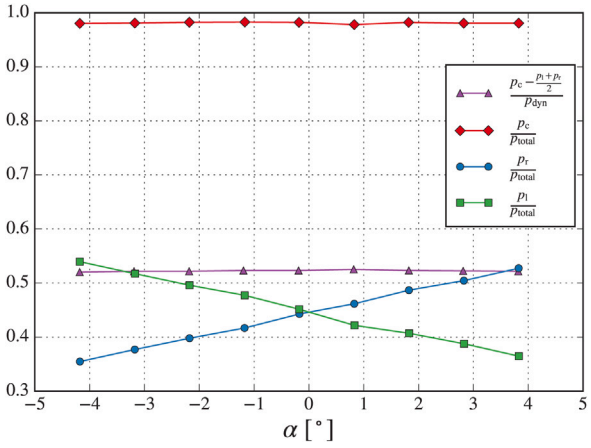

Fig. 15. Calibration of traverse probe: p_l and p_r are pressure at side holes, p_c is pressure at central hole, p_{total} and p_{dyn} are total and dynamic pressures.

520 mm, with an outer diameter equal to 6.0 mm. The probe end was of cobra type (L-shaped). The angles of the two side holes with respect to the central hole were about 45°. The probe was calibrated in uniform steady flow against a standard Pitot tube at the exit from a wind tunnel. The calibration curves are shown in Fig. 15. Naturally, this calibration did not cover strongly non-uniform shear-flow conditions, especially close to walls and downstream of rotor blades and guide vanes.

Flow angle, total and dynamic pressures were measured using the null technique with the probe's moving mechanism. In the null technique, the probe is first aligned with the flow such that the pressure difference between the side holes is zero, $p_l - p_r = 0$. The total and dynamic pressures are then obtained from the application of the calibration coefficients p_c/p_{total} and $(p_c - (p_l + p_r)/2)/p_{dyn}$ to the measurements of the pressure at the central (p_c) and side holes, Fig. 15.

5.2. Instrumentation

The measurements included rotational speed, shaft torque, and pressures. For pressure measurements, five Furness Controls differential micromanometers of model FC012 were used, covering, in their main and secondary scales, the ranges from 1999 down to 1.999 mm H_2O.

The used Vibro-Meter TG-5/BP torque transducer could read values up to 50 Nm, which was enough even for torque peaks that occurred during fast velocity variations. The rotational speed was measured by a photoelectric cell incorporated into the torque transducer.

The differential pressure manometers with different pressure ranges were calibrated against a Betz manometer, and were selected depending on the expected pressure range.

Table 3
Uncertainty of the instruments.

Variable	Model	Range	Accuracy
Static pressure	Furness FC012	±1.999 mm H_2O	±0.5% of reading
Static pressure	Furness FC012	±19.99 mm H_2O	±0.5% of reading
Static pressure	Furness FC012	±199.9 mm H_2O	±0.5% of reading
Static pressure	Furness FC012	±1999 mm H_2O	±0.5% of reading
Torque	Vibro-Meter TG-5/BP	±50 Nm	±0.5%FSO
Rotational speed	Vibro-Meter ML103	±3000 rpm	±0.1 rpm
Atmospheric pressure	Testo 551	–	±300 Pa
Air temperature	Testo 175T1	−20 to +55°C	±0.1°C
Air humidity	Testo 175T1	0 to 100 %rH	±2 %rH

In all instruments, the output signal voltage was converted into the proper unit (e.g. voltage into pressure). Table 3 presents the uncertainty of the instruments. The air flow was assumed incompressible throughout the experiments.

The analogue signals from the devices described above converged to an acquisition data card DAQCard-6024E from National Instruments. The signal acquisition frequency was 100 Hz and the number of samples was 1000, which means that the final value for each measured quantity was a time-averaged value over a time span of 10 s. The LabView software was the platform to gather and treat the experimental data.

After a warm-up period of about 30 min with the blades removed from the two rotors, the bearing friction torque, assumed negative, was measured separately as a function of the rotational speed up to 3000 rpm. That value was subtracted from the total measured torque in order not to affect the aerodynamic performance of the turbine by a power loss that depended on the test-rig bearings.

6. Experimental results

6.1. Overall performance

The experimental results for the turbine performance are expressed in terms of the dimensionless flow rate coefficient Φ (defined in Eq. (17)), the dimensionless pressure head coefficient Ψ, the dimensionless power output coefficient Π and the turbine efficiency η, defined as

$$\Psi = \frac{\Delta p}{\rho \Omega^2 D^2}, \quad \Pi = \frac{T}{\rho \Omega^2 D^5}, \quad \eta = \frac{\Pi}{\Phi \Psi}. \tag{19}$$

Here, ρ is air density, D is turbine diameter, $\Delta p = p_{at} - p_{pl}$ is pressure head defined as atmospheric pressure p_{at} minus pressure p_{pl} in the (upstream part of) the plenum chamber, and T is torque.

Plots of efficiency η and pressure head coefficient Ψ versus flow rate coefficient Φ at different rotational speeds are shown in Fig. 16 versus flow rate coefficient Φ, for the turbine with and without guide vanes.

The rotational speed varied between 1300 rpm (Ω = 136 rad/s) and 2750 rpm (Ω = 288 rad/s). The corresponding values of the Reynolds number $Re = \rho \Omega D^2/\mu$ (μ is dynamic viscosity) are 3.2×10^6 and 6.8×10^6.

An uncertainty analysis has been carried out for the experimental results, following the procedures described in Ref. [33]. Uncertainty values (95% confidence) u_η and u_Ψ, for the efficiency η and dimensionless pressure head Ψ, respectively, appear in Table 4 for the two turbines and for several values of the dimensionless flow rate coefficient Φ. Those uncertainty values are also shown in Fig. 16.

It may be seen, in all four parts of Fig. 16, that the plotted points, obtained for different values of the rotational speed, are fairly well aligned along a single line. This may be explained by the Reynolds number having been large enough for it not to significantly affect the turbine performance.

The curve Ψ(Φ) represents, in dimensionless form, the damping provided by the turbine. In both cases, with a good approximation, the curve is a straight line through the origin $\Psi = K\Phi$ (with some deviations if Φ exceeds the stall-free limit), which confirms the biplane

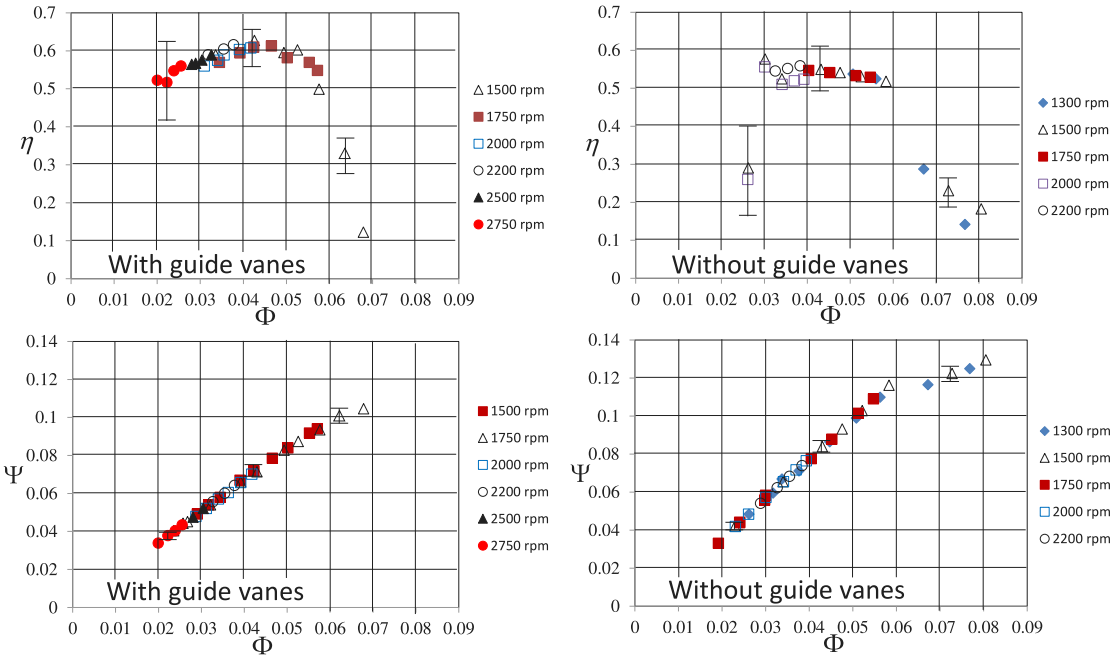

Fig. 16. Measured values of efficiency η and dimensionless pressure head coefficient Ψ versus dimensionless flow rate coefficient Φ, for the turbine with and without guide vanes. Uncertainty limits are shown for some values of Φ.

Table 4
Uncertainty of measured results.

Turbine	Φ	u_η	u_Ψ
With GV	0.0212	0.1260	0.0022
	0.0424	0.0579	0.0027
	0.0636	0.0468	0.0047
No GV	0.0276	0.1340	0.0022
	0.0424	0.0581	0.0045
	0.0636	0.0310	0.0053

Wells turbine (with or without guide vanes) as a linear turbine (a characteristic of Wells turbines in general). The presence of the guide vanes significantly affects the coefficient K, with $K = 1.65$ for the turbine with guide vanes and $K = 1.98$ for the turbine without guide vanes. This qualitatively agrees with the findings of the two-dimensional analysis in Section 2.

The presence of the guide vanes also significantly affects the efficiency curve $\eta(\Phi)$. The peak efficiency increases from about 0.55 to about 0.62. The sharp drop in efficiency occurs at a higher value of Φ if no guide vanes are present, whereas the turbine with guide vanes is more efficient for the relatively small values of Φ.

It may be of interest to compare these experimental results with the numerical results published in Ref. [22] with a CFD code for the solution of the Reynolds-Averaged-Navier–Stokes (RANS) equations. In that paper, the authors adopted the same geometry for the rotors as in the present experimental investigation. However, the gap between rotor planes, and especially the geometry of the guide vane system, are different from those adopted here. In Ref. [22], the circular-arc profile of the guide vanes is spanwisely invariant, with a chord length of 90 mm and an angle $\gamma = 30°$ (as defined in Fig. 6). The gap between rotor planes is $G = 187.5$ mm for the turbine without guide vanes and $G = 180$ mm for the turbine with guide vanes. Numerical results are plotted in Fig. 17. The peak efficiency is 0.63 with guide vanes and 0.62 without guide vanes, a smaller difference compared with the experimental results. This may be partly explained by the simple two-dimensional geometry of the guide vanes adopted in the numerical modelling. As explained in Section 3, the guide vanes of

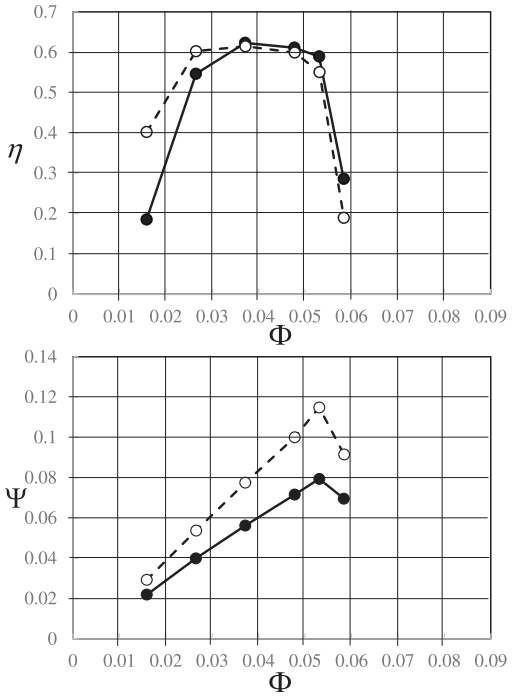

Fig. 17. Efficiency η and dimensionless pressure head coefficient Ψ versus dimensionless flow rate coefficient Φ, for the turbine with guide vanes (solid lines) and without guide vanes (broken lines). Results from numerical modelling [22].

the tested turbine had a three-dimensional configuration to match the spanwisely varying flow angle at the exit from the upstream rotor. As in the experimental results, in the stall-free region, the curves of Ψ versus Φ are approximately straight lines through the origin, with slope $K = \Psi/\Phi$ equal to 1.53 and 2.07 for the turbines with and without guide vanes, respectively. These results should be compared with the measured values 1.65 and 1.98 (see above).

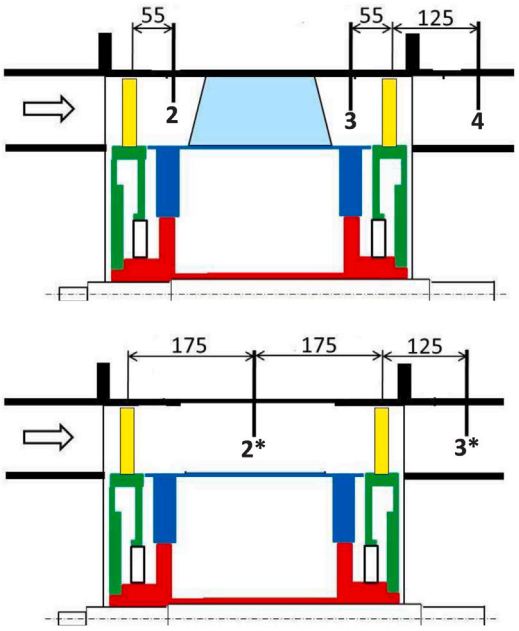

Fig. 18. Locations of the traverse probe (dimensions in mm).

Both the numerical modelling and the experiments show that the presence of the guide vanes produces a decrease in the slope of the (approximately straight) curve of Ψ versus Φ. It also produces an increase in the peak efficiency: from 0.55 to 0.62 (experiments) and from 0.62 to 0.63 (numerical model). The modest increase exhibited by the results from the numerical model may be a consequence of the simplified aerodynamic design of the guide vanes.

6.2. Traverse probe measurements

The traverse probe was used to measure total pressures, absolute velocities and flow angles on several duct sections of the two turbine configurations and for several values of the dimensionless flow rate Φ. These sections were located as follows (see also Fig. 18). Biplane with guide vanes: duct section 2 between the first rotor and the guide vane row, 55 mm downstream of the first rotor plane; duct section 3 between the guide vane row and the second rotor, 55 mm upstream of the second rotor plane; duct section 4 125 mm downstream of the second rotor plane. Biplane without guide vanes: duct section 2* equidistant from the two rotor planes; duct section 3* 125 mm downstream from the second rotor.

Assuming time-invariant flow rate and rotational speed, the (relative) velocity field in the vicinity of the first rotor may be considered steady and circumferentially periodic in a rotating frame of reference (if turbulent fluctuations are neglected). The time-averaged signal from the fixed probe located downstream of the same rotor (duct section 2) is directly related, through the blade velocity **U**, to the circumferential average of the relative flow velocity: it is represented by vector $\mathbf{V}_2$ in the two-dimensional cascade of Fig. 5. On duct section 3, downstream of the guide vanes, the flow is assumed circumferentially periodic, and a circumferential mass average should be taken over an angular pitch of the guide-vane row, in order to obtain velocity vector $\mathbf{V}_3$ shown in Fig. 5. This is why, on duct section 3, several (in fact five) traverses were made with the three-hole probe, covering one circumferential pitch of the guide-vane row. The flow angle, as well as the axial component of the flow velocity and the total pressure (in dimensionless form) are shown versus z^* in Figs. 19 and 20, where z^* is a dimensionless spanwise coordinate defined as

$$z^* = \frac{r - r_{\text{hub}}}{R - r_{\text{hub}}}. \tag{20}$$

Here r is the distance to the rotational axis, $R = D/2$ and r_{hub} is the hub radius. In these figures, zero angle means axial flow (no swirl), and so the plotted angles should be understood as equal to $\alpha - 90°$, where α is the angle represented in the velocity triangles of Figs. 4 and 5. The axial flow velocity is plotted in dimensionless form as $V_x^\star = V_x/\bar{V}$, where $\bar{V}$ is the averaged velocity defined as the volume flow rate Q divided by the cross-sectional area. The dimensionless total pressure is defined as $p_0^\star = p_0/(\rho\Omega^2 D^2)$.

In duct sections 2 and 3 of the angle plots shown in Fig. 19, the broken line represents the absolute flow velocity angles upstream and downstream of the guide vanes that had been adopted in the design of those vanes and appear in Table 2.

The comparison, on duct section 2, of the measured curves $\Phi_1 = 0.0212$ and $\Phi_2 = 0.0424$ with the broken line shows a fairly good agreement (especially for Φ_2) in the central region. However, the differences are markedly larger closer to the duct walls, which should be explained by boundary layer and secondary flow effects. (It should also be mentioned that the directional probe calibration did not include shear flows.) The larger differences between the curve $\Phi_3 = 0.0636$ and the broken line should be expected, since this occurs in fully stalled flow conditions at the first rotor.

The comparison of flow angles on duct section 3 (downstream of the guide vanes) with the broken line should give an indication of the quality of the guide-vane design. The three experimental curves are almost coincident in the central region, with an excessive deflection of about five degrees with respect to the design (broken) curve.

A comparison between the results on duct section 3* (exit flow from the biplane turbine without guide vanes, Fig. 20) and on duct section 4 (exit flow from the biplane turbine with guide vanes, Fig. 19) shows that the guide vanes provide an effective reduction in the swirl of the turbine exit flow, especially under non-stalled conditions (Φ_1 and Φ_2). Naturally, the reduction in the exit kinetic energy associated with the swirl component of the velocity was accompanied by the energy loss in the guide vanes. Whether this balance is positive or negative may be found from the comparison of the efficiency curves in Fig. 16 (see also the following subsection).

In the definition of turbine efficiency, the available pressure head was assumed as the difference between atmospheric pressure and plenum pressure. In fact, there are energy losses in the entrance duct, as shown in the velocity profile of Fig. 21. The velocities were measured with a Pitot tube located 110 mm upstream of the first rotor plane. It may be seen that the boundary layer is thicker close to the external duct as compared with what occurs at the hub. This may be explained by flow separation at the entrance edge of the outer casing located 830 mm upstream of the first rotor plane (note that the hub is much longer than the outer duct), Fig. 12. The relatively thick boundary layer can partly explain the three-dimensional flow characteristic, and the secondary flow effects present downstream of the first rotor, which in Figs. 19 and 20 appear with greater intensity and evidence on the casing side of the turbine.

6.3. Integral parameters and loss coefficients

Quantities such as energy balances, efficiencies and loss coefficients can be determined from the data acquired by the traverse moving probe.

The biplane rotor with guide vanes is considered first. The torque T_{R1} on the first rotor may be computed as

$$T_{\text{R1}} = -2\pi\rho \int_{r_{\text{hub}}}^{R} V_{2x}(r)\, V_{2\theta}(r)\, r^2 \, \mathrm{d}r, \tag{21}$$

where r is the radial coordinate, the subscripts x and θ stand for axial and circumferential components of the velocity, respectively, and the flow upstream of the first rotor is assumed swirl-free. Identically, for the torque T_{R2} on the second rotor, it is

$$T_{\text{R2}} = 2\pi\rho \int_{r_{\text{hub}}}^{R} \left[V_{3x}(r)\, V_{3\theta}(r) - V_{4x}(r)\, V_{4\theta}(r)\right] r^2 \, \mathrm{d}r. \tag{22}$$

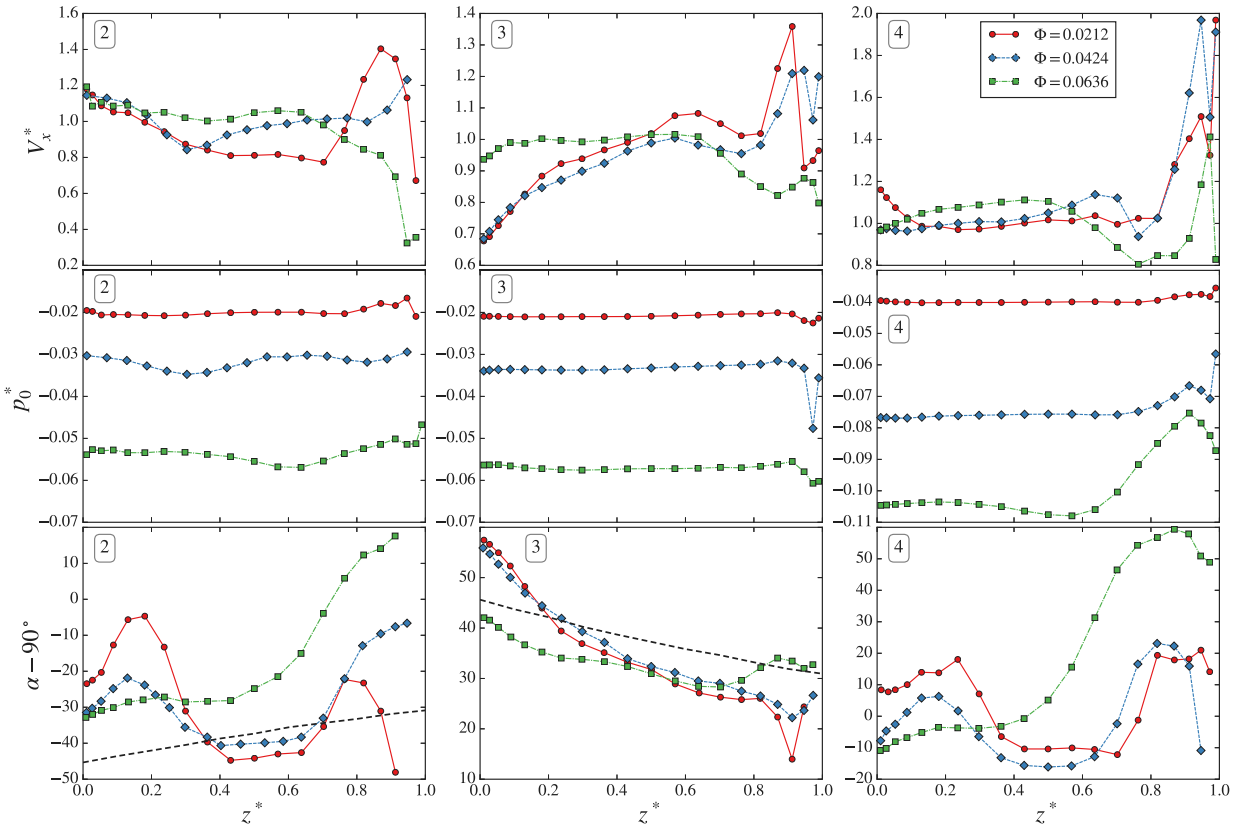

Fig. 19. Dimensionless plot of measured values of the absolute flow velocity angle α, axial flow velocity $V_x^\star$ and total pressure $p_0^\star$ versus dimensionless spanwise coordinate $z^\star$ for the biplane turbine with guide vanes: (2) downstream of the first rotor; (3) between the guide vanes and the second rotor: (4) downstream of the second rotor. Solid lines: measured values; broken line: design values for the guide vane angles.

The power $P_{\text{loss,R1}}$ lost in the first rotor is

$$P_{\text{loss,R1}} = \dot{E}_{12} - \Omega T_{\text{R1}}, \tag{23}$$

where

$$\dot{E}_{12} = 2\pi \int_{r_{\text{hub}}}^{R} \left[V_{1x}(r) p_{01}(r) - V_{2x}(r) p_{02}(r)\right] r \, \mathrm{d}r \tag{24}$$

is the power available to the first rotor. In Eq. (24), p_{01} is the total pressure upstream of the first rotor, measured with the Pitot tube, and p_{02} is the total pressure downstream of the first rotor, measured by the directional probe.

The power lost upstream of the first rotor (entrance duct) is

$$P_{\text{loss,Inlet}} = 2\pi \int_{r_{\text{hub}}}^{R} V_{1x}(r) \left[p_{\text{at}} - p_{01}(r)\right] r \, \mathrm{d}r \tag{25}$$

where p_{at} is the atmospheric pressure.

The power lost in the guide vanes is

$$P_{\text{loss,GV}} = 2\pi \int_{r_{\text{hub}}}^{R} \left[V_{2x}(r)\, p_{02}(r) - V_{3x}(r)\, p_{03}(r)\right] r \, \mathrm{d}r. \tag{26}$$

The power $P_{\text{loss,R2}}$ lost in the second rotor is

$$P_{\text{loss,R2}} = \dot{E}_{34} - \Omega T_{\text{R2}}, \tag{27}$$

where

$$\dot{E}_{34} = 2\pi \int_{r_{\text{hub}}}^{R} \left[V_{3x}(r) p_{03}(r) - V_{4x}(r) p_{04}(r)\right] r \, \mathrm{d}r \tag{28}$$

is the power available to the second rotor.

Finally, the power lost downstream of the second rotor is

$$P_{\text{loss,Exit}} = 2\pi \int_{r_{\text{hub}}}^{R} V_{4x}(r) \left[p_{04}(r) - p_{\text{pl}}\right] r \, \mathrm{d}r\,. \tag{29}$$

Table 5
Loss coefficients and efficiency of the turbine with guide vanes.

Φ	Λ_{Inlet}	Λ_{R1}	Λ_{GV}	Λ_{R2}	Λ_{Exit}	η^*	η
0.0212	0.005	0.143	0.029	0.212	0.051	0.560	0.544
0.0424	0.006	0.148	0.029	0.159	0.073	0.585	0.629
0.0636	0.007	0.325	0.036	0.295	0.146	0.191	0.223

Here, p_{pl} is the pressure in the upstream part of the plenum chamber. Note that losses between the exit from the second rotor and the plenum chamber are essentially kinetic energy losses.

It is convenient to introduce a dimensionless power loss as

$$\Pi_{\text{loss}} = \frac{P_{\text{loss}}}{\rho\, \Omega^3 D^5}, \tag{30}$$

and dimensionless loss coefficients as

$$\Lambda = \frac{\Pi_{\text{loss}}}{\Pi_{\text{avai}}}, \tag{31}$$

where $\Pi_{\text{avai}} = \Phi\Psi$ is the dimensionless power available to the turbine-based on the available pressure head Δp between the atmosphere and the plenum chamber. The turbine efficiency evaluated in this way is

$$\eta^* = 1 - \Lambda_{\text{Inlet}} - \Lambda_{\text{R1}} - \Lambda_{\text{GV}} - \Lambda_{\text{R2}} - \Lambda_{\text{Exit}}. \tag{32}$$

In a similar way, rotor loss coefficients and turbine efficiency may be defined and computed for the turbine without guide vanes.

Table 5 shows the results of loss coefficients Λ and efficiency η^* for three values of the dimensionless flow rate Φ. Values of the efficiency η from measurements of the torque and rotational speed are also shown for comparison. Results for the turbine without guide vanes appear in Table 6. In general, the two calculation methods gave for the efficiency values η and η^* that are not substantially different.

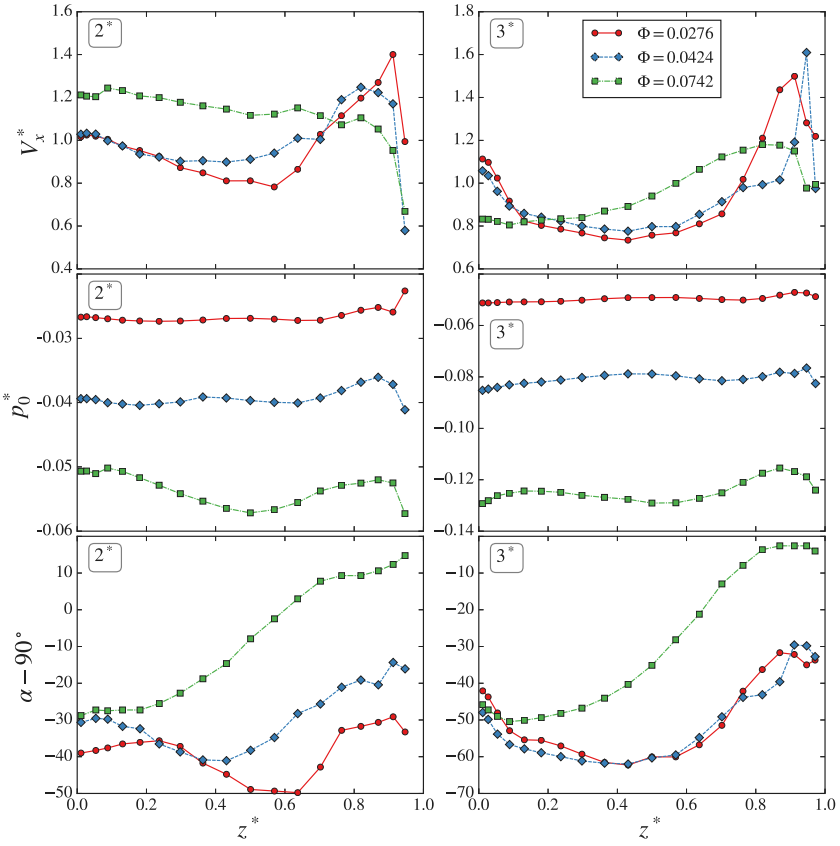

Fig. 20. Dimensionless plot of the absolute-flow velocity angle α, axial flow velocity $V_x^\star$ and total pressure $p_0^\star$ versus dimensionless spanwise coordinate $z^\star$ for the biplane turbine without guide vanes: (2*) downstream of the first rotor; (3*) downstream of the second rotor.

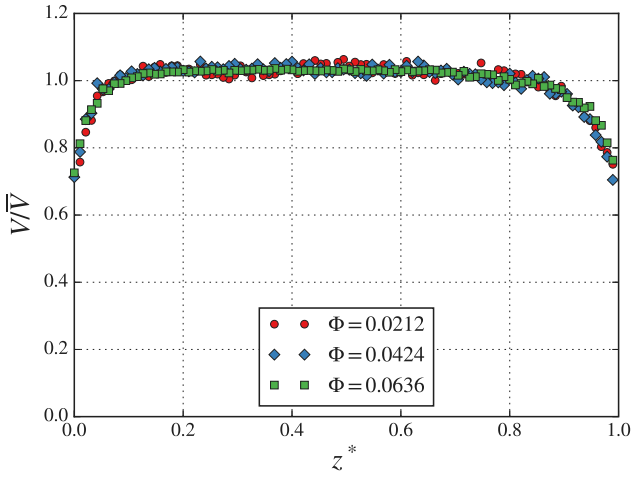

Fig. 21. Dimensionless plot of the flow velocity 110 mm upstream of the first rotor versus dimensionless spanwise coordinate $z^\star$.

Tables 5 and 6 seem to show that, for fixed Φ, the presence of the guide vanes significantly changes the losses in the first rotor (especially in the unstalled regime). This may be partly explained by the definitions of the dimensionless loss coefficients in Eq. (31), more precisely the division by Π_{avai}, and by the different distances from the first rotor to where the measurements were made. Fig. 16 shows that, for given Φ, the presence of the guide vanes results in a decrease in the value of $\Pi_{avai} = \Phi\Psi$. For the purpose of comparing losses in the homologous parts of the two turbines, it is preferable, instead of Λ, to introduce the dimensionless loss coefficients

$$\lambda_{R1} = \frac{\Pi_{loss,R1}}{\Phi}, \quad \lambda_{GV} = \frac{\Pi_{loss,GV}}{\Phi}, \quad \lambda_{R2} = \frac{\Pi_{loss,R2}}{\Phi}. \tag{33}$$

Loss coefficients λ are plotted in Fig. 22 versus dimensionless flow rate Φ for the rotors and guide vanes of the two turbines. The losses in the guide vanes were much smaller than those in the rotors, which is not surprising, since, in a biplane Wells turbine with guide vanes, the relative flow velocity about the rotor blades is much larger than the absolute flow velocity in the guide vane row. In unstalled conditions ($\Phi < 0.045$), the presence of the guide vanes greatly decreased the losses downstream of the second rotor, as should be expected, since the kinetic energy associated with swirl in the exit flow was greatly reduced. Also the losses in the first and second rotor of both turbines were not very different from each other. The performance of the second

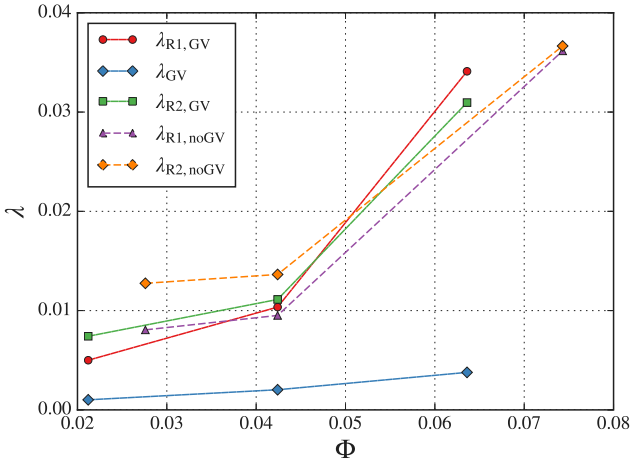

Fig. 22. Dimensionless power loss λ versus dimensionless flow rate Φ.

Table 6
Loss coefficients and efficiency of the turbine without guide vanes.

Φ	Λ_{Inlet}	Λ_{R1}	Λ_{R2}	Λ_{Exit}	η^*	η
0.0276	0.005	0.177	0.280	0.077	0.461	0.501
0.0424	0.005	0.136	0.195	0.134	0.530	0.544
0.0743	0.006	0.295	0.299	0.146	0.254	0.234

rotor in the stalled regime was not improved by the presence of the guide vanes.

7. Turbine performance in bidirectional flow

7.1. Unidirectional versus bidirectional flow testing

Wells turbines and other self-rectifying air turbines that equip OWC wave energy converters are subject to bidirectional oscillating flow. Unlike in bidirectional flow test rigs (usually equipped with a reciprocating piston [34]), this could not be directly simulated in the blow-down rig used in the model-tests reported here. The validity of these tests is based on several assumptions: (i) the turbine performance is not significantly affected if the flow direction is reversed; (ii) the turbine performance under time-varying flow rate (and possibly varying rotational speed) may be represented by the measured performances for a sufficiently large set of flow rates and rotational speeds covering the working situations in real sea conditions; (iii) the flow admitted to the turbine is swirl-free.

Condition (i) requires the turbine and the duct connections to the atmosphere and to the OWC air chamber to be symmetrical with respect to a plane perpendicular to the rotational axis. This is assumed to be the case here, but is not necessarily true in a full-sized plant.

Condition (ii) is associated with two frequencies: (a) a representative wave frequency f_{wave} and (b) a rotor blade passing frequency $f_{\text{rotor}} = \Omega Z/(2\pi)$, where Z is the number of blades in each rotor. Condition (ii) is met if f_{rotor} is very large compared with f_{wave}, which in general occurs in OWC converters. In the Mutriku OWC-breakwater plant equipped with biplane Wells turbines, it is $f_{\text{wave}} \simeq 0.1\,\text{s}^{-1}$, $\Omega \simeq 300\,\text{rad/s}$, $Z = 5$, $f_{\text{rotor}} \simeq 240\,\text{s}^{-1}$ and $f_{\text{rotor}}/f_{\text{wave}} = \mathcal{O}(10^3)$ [35].

7.2. Swirl inhalation

Flow reversal happens twice in a wave cycle when the flow rate Q changes sign. Depending on the shape and length of the ducts that connect the turbine to the air chamber and to the atmosphere, the air contained in the connecting duct at the time of flow reversal and subsequently admitted to the turbine has a swirling component induced by the previous passage of the same air particles through the turbine. This may affect the turbine performance during (possibly short) intervals of time following flow reversal. This effect was detected during exhalation in bidirectional flow tests of a monoplane Wells turbine without guide vanes in a rig equipped with a reciprocating piston [36]. Naturally, such effect is reduced if the turbine is provided with guide vanes whose object is precisely to reduce energy losses by swirl at turbine exit. Besides, it takes place, after flow reversal, during a time interval likely to be small compared with the wave period, when the power available to the turbine is relatively small.

During exhalation, the air flow is expected to lose most of its swirl in the atmosphere by turbulent diffusion and wind effect. This was confirmed in the experiments reported in Ref. [36]. In what follows, this is assumed to be the case. To investigate this effect, we consider the duct, assumed approximately cylindrical, that connects the turbine to the atmosphere. Its cross-sectional area is denoted by $A(x)$, where x is the axial distance from the duct opening. The volume flow rate of air is assumed to be a given function of time $Q(t)$, with $Q(0) = 0$ at the instant of flow reversal and $Q > 0$ when the air flows into the turbine. The section-averaged value of the axial flow velocity component is $Q(t)/A(x)$. Consider a 'representative' fluid particle moving along the duct. At time t, the distance of the particle from the duct opening is denoted by $\xi(t)$, with $\xi(0) = 0$. The axial component of the particle velocity is assumed approximately equal to the volume flow rate divided by the local cross-sectional area of the duct

$$\frac{\mathrm{d}\xi}{\mathrm{d}t} = \frac{Q(t)}{A(\xi)}\,. \tag{34}$$

Integration gives

$$\int_0^{\xi} A(\xi)\,\mathrm{d}\xi = \int_0^{t} Q(t)\,\mathrm{d}t. \tag{35}$$

Since $A(x)$ and $Q(t)$ are supposed to be known functions, Eq. (35) yields the time t as a function of distance ξ. If ξ is taken equal to the total length L of the duct, the left-hand-side of Eq. (35) is equal to the total volume $\mathcal{V}$ of the duct, and the time τ that the particle takes to travel the whole length L of the duct may be obtained. If the turbine pressure head Δp is known as a function of the flow rate Q, the energy available to the turbine during that time interval may be computed by simple integration, and compared with the energy available during one-half of the wave period.

We apply this reasoning to the tested biplane turbine without guide vanes, and assume $Q(t) = Q_{\text{max}} \sin \omega t$, where ω is the radian frequency of the waves and Q_{max} is taken equal to the maximum stall-free flow rate through the turbine at the adopted rotational speed. Upon integration, Eq. (35) gives

$$\tau = \frac{1}{\omega} \arccos\left(1 - \frac{\omega \mathcal{V}}{Q_{\text{max}}}\right). \tag{36}$$

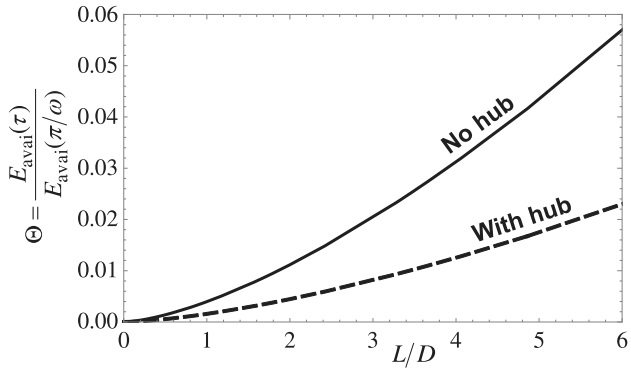

Fig. 23. Ratio Θ between energy $E_{\text{avai}}(\tau)$ available to the turbine during swirl inhalation $(0 < t < \tau)$ and energy $E_{\text{avai}}(\pi/\omega)$ available during half-wave-period $(0 < t < \pi/\omega)$, versus L/D (L is duct length and D is turbine diameter). Solid line: duct without hub; broken line: turbine hub extended along the duct.

Fig. 16 yields $K = \Psi/\Phi = 1.98$ and $\Phi_{\max} = 0.060$. It is $D = 0.590\,\text{m}$, and we take $\rho = 1.25\,\text{kg/m}^3$. To find realistic values for the rotational speed Ω and the wave radian frequency ω, the tested turbine is assumed roughly as a reduced model of the biplane Wells turbines that equip the OWC-breakwater plant in Mutriku, Northern Spain, whose rotor diameter is 0.75 m, i.e., turbine scale is $\varepsilon_{\text{t}} = 0.59/0.75 = 0.787$. Typical values for Mutriku plant are wave period 10 s ($\omega_{\text{Mut}} = 0.628$) and rotational speed 3000 rpm ($\Omega_{\text{Mut}} = 314\,\text{rad/s}$) [35,37]. Applying dimensional analysis to the whole OWC converter (hydrodynamics and aerodynamics, [38]), we find, for the Froude scale, $\varepsilon = \varepsilon_{\text{t}}$, and, for the tested turbine, $\Omega = \Omega_{\text{Mut}}\,\varepsilon_{\text{t}}^{-1/2} = 354\,\text{rad/s}$ (turbine rotational speed) and $\omega = \omega_{\text{Mut}}\,\varepsilon^{-1/2} = 0.708\,\text{rad/s}$ (radian frequency of air flow oscillation). From Eqs (17) and (19), and $K = 1.98$, we find $Q_{\max} = 4.36\,\text{m}^3/\text{s}$, $k = \Delta p/Q = 1.49\times10^3\,\text{Pa s/m}^3$, and, for the pneumatic power available to the tested turbine, $P_{\text{avai}}(t) = k(Q(t))^2$. The energy $E_{\text{avail}}(t)$ available to the turbine during the interval $(0, t)$ may be obtained by integration and is

$$E_{\text{avai}}(t) = kQ_{\max}^2\left[\frac{t}{2} - \frac{1}{4\omega}\sin 2\omega t\right]. \tag{37}$$

During one-half of the wave period, π/ω, it is

$$E_{\text{avai}}(\pi\omega^{-1}) = \frac{k\pi}{2\omega}Q_{\max}^2. \tag{38}$$

Fig. 23 shows results for a cylindrical duct with diameter D equal to the turbine diameter. The ratio $\Theta = E_{\text{avai}}(\tau)/E_{\text{avai}}(\pi/\omega)$, between the energy available to the turbine during swirl inhalation $(0 < t < \tau)$ and the energy available during half-wave-period $(0 < t < \pi/\omega)$, is plotted versus L/D (L is duct length and D is turbine diameter). In the figure, the solid line concerns a duct without hub; in the geometry represented by the broken curve, the turbine hub extends along the duct. Fig. 23 shows that the swirl-swallowing effect is expected to be practically negligible ($\Theta < 0.01$) if $L/D < 2$ (no hub in the duct) or $L/D < 4.5$ (duct with hub).

The situation concerning the occurrence of swirl at the turbine entrance during exhalation requires careful analysis. In the test rig described in Ref. [36], the air chamber in a real full-sized OWC converter was represented by a circular cylinder coaxial with the turbine. A piston in reciprocating motion stood for the moving free-surface inside a real OWC. This topology is in general not expected to be an accurate representation of what happens in the air chamber of a real OWC converter, especially if the turbine is not coaxial with the air chamber. On the other hand, no measurements of swirl in the turbine duct of an OWC plant under real sea conditions seem to have been reported. It may be concluded that eventual swirl inhalation by the turbine during the exhaust period needs further investigation.

7.3. Average performance in irregular waves

The curves in Fig. 16 reproduce, in dimensionless form, the performance of the turbine in steady conditions. The averaged performance of the turbine in an OWC acted upon by irregular waves may be a more interesting indicator in the process of turbine design or selection. This may be done through a stochastic approach, see Refs. [13,39]. The water surface elevation of real-sea waves, as well as the air pressure oscillation in the OWC chamber, may be regarded as random processes. For most engineering purposes, the sea surface motion may be considered as a stochastic Gaussian process [40]. The same may be said of the air pressure oscillation Δp, provided that the OWC converter is a linear system. More precisely, (i) if linear water wave theory is applicable to the hydrodynamic process of wave energy absorption; (ii) if the oscillations in air pressure are (in modulus) small compared with the atmospheric pressure; and (iii) if the turbine is linear (flow rate proportional to pressure head). Condition (iii) is met with good approximation by Wells turbines at constant rotational speed.

Let σ be the standard deviation or root-mean-square (rms) of the pressure oscillation Δp. If Δp is Gaussian, then its probability density function is [41]

$$f_{\Delta p}(\Delta p) = \frac{1}{\sqrt{2\pi}\sigma}\exp\frac{-(\Delta p)^2}{2\sigma^2} \tag{39}$$

or, in dimensionless form,

$$f_{\Psi}(\Psi) = \frac{1}{\sqrt{2\pi}\sigma_{\Psi}}\exp\frac{-\Psi^2}{2\sigma_{\Psi}^2}, \tag{40}$$

where Ψ is the dimensionless pressure head defined by Eq. (19), and

$$\sigma_{\Psi} = \frac{\sigma}{\rho\,\Omega^2 D^2}. \tag{41}$$

The efficiency $\eta(\Psi)$ and the dimensionless flow rate $\Phi(\Psi)$ are assumed here to be known functions of Ψ. In dimensionless form, the available power and the power output are $\Pi_{\text{avai}}(\Psi) = \Phi(\Psi)\,\Psi$ and $\Pi(\Psi) = \eta(\Psi)\,\Phi(\Psi)\,\Psi$, respectively. Their averaged values, denoted by an overbar, are

$$\left\{\bar{\Pi}_{\text{avai}}(\sigma_{\Psi}), \bar{\Pi}(\sigma_{\Psi})\right\} = \frac{1}{\sqrt{2\pi}\sigma_{\Psi}}\int_{-\infty}^{\infty}\left\{\Phi(\Psi)\,\Psi, \eta(\Psi)\,\Phi(\Psi)\,\Psi\right\}\exp\frac{-\Psi^2}{2\sigma_{\Psi}^2}\,\mathrm{d}\Psi. \tag{42}$$

Note that, if the turbine and connecting ducts are symmetric with respect to a plane perpendicular to the rotational axis, the integrand in Eq. (42) is an even function of Ψ; this is assumed to be the case here. The presence of the exponential function allows a relatively small interval of integration to be adopted in numerical calculations. The averaged efficiency is defined as

$$\bar{\eta}(\sigma_{\Psi}) = \frac{\bar{\Pi}(\sigma_{\Psi})}{\bar{\Pi}_{\text{avai}}(\sigma_{\Psi})}. \tag{43}$$

The stochastic approach was applied to the experimental results from the tests of the biplane Wells turbine with and without guide vanes. Time-independent rotational speed is assumed. The volume flow

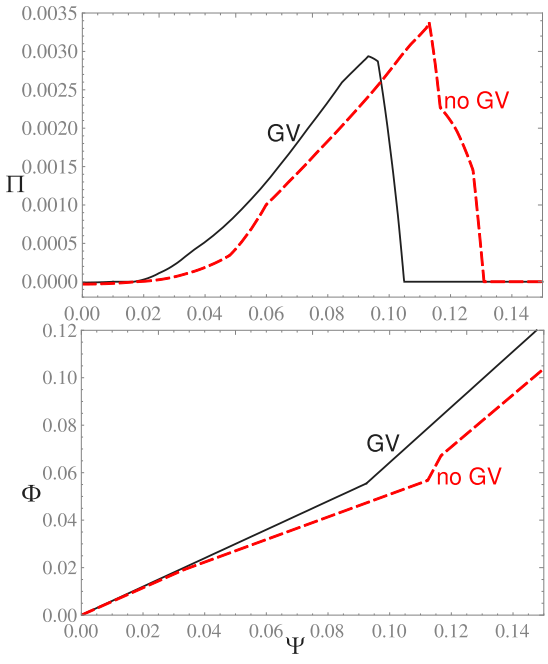

Fig. 24. Turbine performance curves: dimensionless power output Π and dimensionless flow rate Φ versus dimensionless pressure head Ψ. Solid lines: turbine with guide vanes; broken lines: turbine without guide vanes.

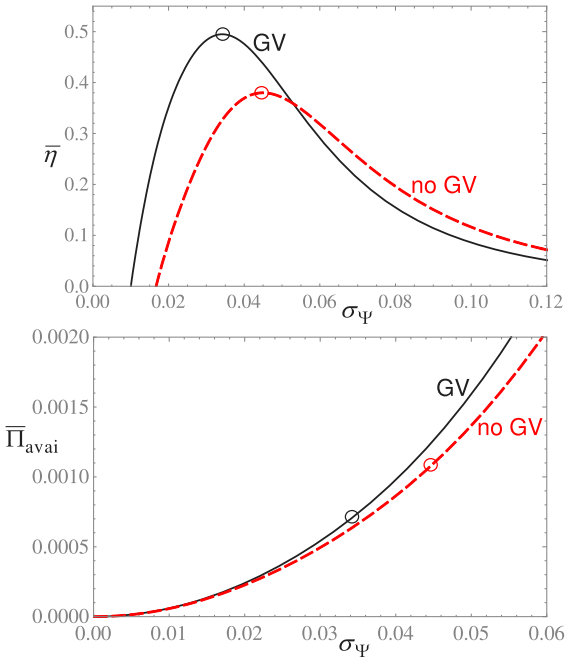

Fig. 25. Dimensionless representation of turbine performance curves in oscillating flow. Averaged efficiency $\bar{\eta}$ and averaged available power $\bar{\Pi}_{avai}$ versus standard deviation (or rms) of pressure head σ_Ψ. Solid lines: turbine with guide vanes; broken lines: turbine without guide vanes. The circles indicate conditions for maximum averaged efficiency.

rate Q, the power output P and the efficiency η are taken as functions of the pressure head Δp. In dimensionless form, this is written as $\Phi(\Psi)$, $\Pi(\Psi)$ and $\eta(\Psi)$. The first function is assumed an odd function, and the other two are even functions of Ψ. Interpolation and extrapolation were used to obtain the performance curves shown in Fig. 24 from the experimental results. In particular, the turbine power output and the efficiency were taken equal to zero under fully stalled conditions. In the figure, the peak power output is larger for the turbine without guide vanes compared with the turbine with guide vanes; this is explained by the larger available power Π_{avai} that occurs in the first case.

The transformation represented by Eq. (42) was applied to the available power Π_{avai} and power output Π of both turbines. The results are plotted in Fig. 25. Several important conclusions may be drawn from this figure. The peak value of the averaged efficiency $\bar{\eta}$ is identified by a circle for each turbine. It is substantially larger for the turbine with guide vanes, 0.49, than for the turbine without guide vanes, 0.38 (ratio $0.49/0.38 = 1.29$). Fig. 25 shows that these peak values occur for different values of σ_Ψ as defined by Eq. (41): $(\sigma_\Psi)_{GV} = 0.342$ and $(\sigma_\Psi)_{noGV} = 0.450$. The same figure gives the corresponding values $(\bar{\Pi}_{avai})_{GV} = 0.000706$ and $(\bar{\Pi}_{avai})_{noGV} = 0.001093$. These two pairs of values may be used to determine the ratio D_{GV}/D_{noGV} between the diameters of the two turbines, and the ratio $\Omega_{GV}/\Omega_{noGV}$ between the rotational speeds of the two turbines, it being assumed that both turbines are designed to fit the same OWC converter subject to the same wave climate (or to the same representative sea state). More precisely, it is specified that both turbines perform at peak efficiency $\bar{\eta}$ (i) for the same design value of σ (standard deviation or root-mean-square of the pressure oscillation Δp), and (ii) for the same design value $\bar{P}_{avai}$ of the averaged power available to the turbine. These conditions may be written in the form of the following system of four equations

$$\begin{aligned}
\frac{\sigma}{\rho\,\Omega_{GV}^2 D_{GV}^2} &= 0.0342,\\
\frac{\sigma}{\rho\,\Omega_{noGV}^2 D_{noGV}^2} &= 0.0450,\\
\frac{\bar{P}_{avai}}{\rho\,\Omega_{GV}^3 D_{GV}^5} &= 0.000706,\\
\frac{\bar{P}_{avai}}{\rho\,\Omega_{noGV}^3 D_{noGV}^5} &= 0.001093,
\end{aligned} \tag{44}$$

which yields the following results

$$\frac{D_{GV}}{D_{noGV}} = 1.01, \quad \frac{\Omega_{GV}}{\Omega_{noGV}} = 1.13. \tag{45}$$

It may be concluded that, if the two turbines are to fit the same OWC converter subject to the same wave climate, their diameters should be approximately equal, while the rotational speed of the turbine with guide vanes should be significantly (about 13%) larger than the rotational speed of the other turbine. The power output ratio is the value 1.29 referred to above.

8. Conclusions

Experiments were carried out in a unidirectional flow rig to investigate the performance improvement of a biplane Wells turbine by the presence of guide vanes between the rotor planes, whose expected role was the reduction in the energy loss due to the swirl kinetic energy at the turbine exit. The guide vanes had a three-dimensional geometry to match the spanwisely varying flow angle at the exit from the upstream rotor and the desired angle for the flow admitted to the second rotor. Overall performance curves were obtained for the turbines with and without guide vanes, as well as flow details, namely flow velocity angles and values, total pressures and energy losses in the components of the two turbines. The experiments were performed in the Reynolds number range between 3.2×10^6 and 6.8×10^6.

It was found that the exit flow angle from the guide vanes fairly well matched the corresponding design value, except close to the hub and outer casing, due to the presence of wall boundary layers and secondary flows. The aerodynamic loss due to kinetic energy at the exit of the biplane Wells turbine was greatly reduced, except under stalled flow conditions at the rotor blades. The energy losses at the guide vanes were found to be small compared with the losses at either of the two rotors.

The presence of guide vanes significantly affected the overall performance of the turbine. The peak efficiency increased from 0.55 to 0.62. The drop in efficiency of the turbine with guide vanes due to stalling was sharper and occurred at a smaller value of the flow rate Φ in comparison with the turbine without guide vanes. On the other hand, the turbine with guide vanes was found to be more efficient in the lower flow-rate range. In both turbine versions, the curves of Ψ versus Φ (dimensionless pressure head versus dimensionless flow rate) were found to be approximately represented by the linear relationship $\Psi = K\Phi$, which is characteristic of Wells turbines in general. The presence of guide vanes significantly decreased K from 1.98 to 1.65, which (for equal rotational speed and diameter) implies a decrease in the damping provided by the turbine.

The experimental results were compared with results in Ref. [22] from numerical modelling of a biplane turbine with and without guide vanes. The two rotors in the biplane were identical to those of the tested turbine, but that was not the case of the guide vanes which were of simple two-dimensional geometry. This may (at least partly) explain the differences in performance, namely the smaller increase of only 0.01 (from 0.62 to 0.63) in peak efficiency provided by the guide vanes.

The used test rig did not provide bidirectional flow. This limitation was discussed, in special on what concerns the influence of the turbine-induced swirl being swallowed by the turbine upon flow reversal. A theoretical simulation revealed that this effect on turbine performance is not expected to be significant unless possibly if the connecting ducts are unusually long.

In real applications, the turbine operates under bidirectional random flow. Such real conditions were simulated by submitting the experimental results to an appropriate mathematical transformation which yielded averaged values for the performance variables. It was found that the presence of the guide vanes increased the averaged efficiency in bidirectional random flow from 0.38 to 0.49. If full-sized versions of two tested models were to be designed to fit the same OWC plant in a given representative sea state, it was found that the diameter of the two turbines should be approximately equal, while the presence of the guide vanes required an increase in rotational speed of about 13%.

CRediT authorship contribution statement

João S. Alves: Investigation, Software, Formal analysis, Data curation, Writing – original draft. **Luís M.C. Gato:** Conceptualization, Methodology, Investigation, Formal analysis, Validation, Writing – original draft, Supervision, Resources, Funding acquisition. **António F.O. Falcão:** Conceptualization, Methodology, Investigation, Formal analysis, Validation, Writing – original draft. **João C.C. Henriques:** Conceptualization, Methodology, Investigation, Formal analysis, Validation, Writing – original draft.

Declaration of competing interest

The authors declare that they have no known competing financial interests or personal relationships that could have appeared to influence the work reported in this paper.

Acknowledgements

This work was partly funded by the Portuguese Foundation for Science and Technology (FCT) through IDMEC, under LAETA, project UIDB/50022/2020 and project MIT-EXPL/SOE/0094/2019.

References

[1] Falcão AFO. Wave energy utilization: A review of the technologies. Renew Sustain Energy Rev 2010;14:899–918. http://dx.doi.org/10.1016/j.rser.2009.11.003.
[2] Heath TV. A review of oscillating water columns. Phil Trans R Soc A 2012;370:235–45. http://dx.doi.org/10.1098/rsta.2011.0164.
[3] Falcão AFO, Henriques JCC. Oscillating-water-column wave energy converters and air turbines: A review. Renew Energy 2016;85:1391–424. http://dx.doi.org/10.1016/j.renene.2015.07.086.
[4] Delmonte N, Barater D, Giuliani F, Cova P. Review of oscillating water column converters. IEEE Trans Ind Appl 2016;52(2):1698–710. http://dx.doi.org/10.1109/TIA.2015.2490629.
[5] Wells AA. Fluid driven rotary transducer. British Patent No. 1595700. 1976.
[6] Babintsev IA. Apparatus for converting sea wave energy into electrical energy. U.S. Patent No. 3922739. 1975.
[7] Raghunathan S. The Wells turbine for wave energy conversion. Prog Aerosp Sci 1995;31:335–86. http://dx.doi.org/10.1016/0376-0421(95)00001-F.
[8] Setoguchi T, Santhakumar S, Maeda H, Takao M, Kaneko K. A review of impulse turbines for wave energy conversion. Renew Energy 2001;23:261–92. http://dx.doi.org/10.1016/S0960-1481(00)00175-0.
[9] Setoguchi T, Takao M. Current status of self-rectifying air turbines for wave energy conversion. Energy Convers Manage 2006;47:2382–96. http://dx.doi.org/10.1016/j.enconman.2005.11.013.
[10] Curran R, Folley M. Air turbine design for OWCs. In: Cruz J, editor. Ocean Wave Energy. Springer, Berlin; 2008, p. 189–219.
[11] Falcão AFO, Gato LMC. Air turbines. In: Sayigh AA, editor. Comprehensive Renewable Energy, vol. 8, Ocean Energy. Elsevier, Oxford; 2012, p. 111–49. http://dx.doi.org/10.1016/B978-0-08-087872-0.00805-2.
[12] Sheata AS, Xiao Q, Saqr KM, Day A. Wells turbine for wave energy conversion: A review. Int J Energy Res 2017;41:6–38. http://dx.doi.org/10.1002/er.3583.
[13] Falcão AFO, Henriques JCC, Gato LMC. Self-rectifying air turbines for wave energy conversion: A comparative analysis. Renew Sustain Energy Rev 2018;91:1231–41. http://dx.doi.org/10.1016/j.rser.2018.04.019.
[14] Falcão AFO, Henriques JCC, Gato LMC, Gomes RPF. Air turbine choice and optimization for floating oscillating-water-column wave energy converter. Ocean Eng 2014;75:148–56. http://dx.doi.org/10.1016/j.oceaneng.2013.10.019.
[15] Raghunathan S, Tan CP. The performance of the biplane Wells turbine. J Energy 1983;7(6):741–2. http://dx.doi.org/10.2514/3.62727.
[16] Raghunathan S, Curran R, Whittaker TJT. The performance of the Islay Wells air turbine. Proc Inst Mech Eng A 1995;209:55–62. http://dx.doi.org/10.1243/PIME_PROC_1995_209_009_02.
[17] Torre-Enciso Y, Ortubia I, López de Aguileta LI, Marqués J. Mutriku wave power plant: From the thinking out to the reality. In: Proc. 8th European Wave Tidal Energy Conference. 2009.
[18] Arena F, Romolo A, Malara G, Fiamma V, Laface V. The first full operative U-OWC plants in the port of Civitavecchia. In: Proc. ASME 36th International Conference on Ocean, Offshore and Arctic Engineering. Trondheim, Norway, 2017, http://dx.doi.org/10.1115/OMAE2017-62036.
[19] Curran R, Gato LMC. The energy conversion performance of several types of Wells turbine designs. Proc Inst Mech Eng A 1997;221:133–45. http://dx.doi.org/10.1243/0957650971537051.
[20] Setoguchi T, Kaneko K, Matsuwei E, Hamakawa H, Matsuki E. Some techniques to improve the performance of biplane Wells turbine for wave power generator. In: Proc. First Pacific/Asia Offshore Mechanics Symposium. 1990, p. 207–12.
[21] Arlitt R, Banzhaf HU, Starzmann R, Biskup F. Air turbine for wave power station. Patent No. WO 2009/089902. 2009.
[22] Das TK, Samad A. The effect of mid-plane guide vanes in a biplane Wells turbine. J Fluids Eng Trans ASME 2019;141(5):051107. http://dx.doi.org/10.1115/1.4041600.
[23] Gato LMC, Falcão AFO. On the theory of the Wells turbine. J Eng Gas Turb Power – Trans ASME 1984;106:628–33. http://dx.doi.org/10.1115/1.3239616.
[24] Gato LMC, Falcão AFO. Performance of Wells turbine with double row of guide vanes. JSME Int J Ser II 1990;33:265–71. http://dx.doi.org/10.1299/jsmeb1988.33.2_265.
[25] von Karman T, Burgers JM. General aerodynamic theory – Perfect fluids. In: Durand WF, editor. Aerodynamic Theory, Vol. 2. Springer, Berlin; 1934.
[26] Weinig FS. Theory of two-dimensional flow through cascades. In: Hawthorne WR, editor. Aerodynamics of Turbines and Compressors. Oxford University Press, Oxford; 1964.
[27] Scholz N. Aerodynamics of Cascades. AGARD-AG-220; 1977.
[28] Lakshminarayana B. Fluid Dynamics and Heat Transfer of Turbomachinery. Wiley, New York; 1996.
[29] Dixon SL, Hall CA. Fluid Mechanics and Thermodynamics of Turbomachinery. 6th ed. Elsevier, Amsterdam; 2010.
[30] Gato LMC, Curran R. Performance of the biplane Wells turbine. J Offshore Mech Arctic Eng–Trans ASME 1996;118(3):210–5. http://dx.doi.org/10.1115/1.2828836.
[31] Schobeiri MT. Turbomachinery Flow Physics and Dynamic Performance. 2nd ed. Berlin: Springer; 2012, http://dx.doi.org/10.1007/978-3-642-24675-3.

[32] Gato LMC, Falcão AFO. Aerodynamics of the Wells turbine. Int J Mech Sci 1988;30:383–95. http://dx.doi.org/10.1016/0020-7403(88)90012-4.
[33] Tavoularis S. Measurement in Fluid Mechanics. Cambridge: Cambridge University Press; 2005.
[34] Das TK, Kumar K, Samad A. Experimental analysis of a biplane Wells turbine under different load conditions. Energy 2020;206:118205. http://dx.doi.org/10.1016/j.energy.2020.118205.
[35] Gato LMC, Henriques JCC, Carrelhas AAD, Lopes BS, Varandas J, Faÿ F-X. OPERA - Open Sea Operating Experience to Reduce Wave Energy Costs, Deliverable D3.3, Turbine and Electrical Equipment Performance and Reliability in Shoreline OWC Wave Plant. 2018, http://opera-h2020.eu/wp-content/uploads/2018/08/OPERA_D3.3_Performancereliability_IST_2018-07-13_v1.0.pdf. [Accessed: 7 July 2021].
[36] Paderi M, Puddu P. Experimental investigation on a Wells turbine under bi-directional flow. Renew Energy 2013;57:570–6. http://dx.doi.org/10.1016/j.renene.2013.02.016.
[37] Carrelhas AAD, Gato LMC, Henriques JCC, Falcão AFO, Varandas J. Test results of a 30 kW self-rectifying biradial air turbine-generator prototype. Renew Sustain Energy Rev 2019;109:187–98. http://dx.doi.org/10.1016/j.rser.2019.04.008.
[38] Falcão AFO, Henriques JCC. Model-prototype similarity of oscillating-water-column wave energy converters. Int J Mar Energy 2014;6:18–34. http://dx.doi.org/10.1016/j.ijome.2014.05.002.
[39] Falcão AFO, Rodrigues RJA. Stochastic modelling of OWC wave power performance. Appl Ocean Res 2002;24:59–71. http://dx.doi.org/10.1016/S0141-1187(02)00022-6.
[40] Goda Y. Random Seas and Design of Maritime Structures. 2nd ed. World Scientific, Singapore; 2000.
[41] Papoullis A, Pillai SU. Probabilities, Random Variables, and Stochastic Processes. 4th ed. McGraw Hill, New York; 2002.